

Analysis of Permanent-Magnet Machine for Sensorless Control Based on High-Frequency Signal Injection

Ji-Hoon Jang, *Student Member, IEEE*, Jung-Ik Ha, *Member, IEEE*, Motomichi Ohto, Kozo Ide, *Member, IEEE*, and Seung-Ki Sul, *Fellow, IEEE*

Abstract—This paper presents the analysis of a surface-mounted permanent-magnet (SMPM) machine for the sensorless control scheme based on the high-frequency fluctuating voltage signal injection method. A simplified high-frequency model of an SMPM machine in the estimated rotor reference frame is developed and a sensorless rotor position and speed estimation algorithm is described. To support this, the high-frequency impedances of an SMPM machine are analyzed by finite-element analysis (FEA) and compared with measurement results using a pulsewidth-modulation (PWM) inverter system under various injection conditions. The results of the FEA and measurements are coincident with each other with some errors due to the nonlinear behavior of the PWM inverter and the SMPM machine. The analysis results give physical insights into selecting the injection conditions for sensorless operation of the SMPM machine even though adjustments considering nonlinear behaviors of PWM inverters are required in the actual operation for the desired performance. The experimental results of speed and position control using a commercial SMPM machine are presented based on the analysis of the SMPM machine for the sensorless control algorithm.

Index Terms—High-frequency signal injection, sensorless operation, surface-mounted permanent-magnet (SMPM) machine.

NOMENCLATURE

Symbols	
K_{err}	Coefficient of rotor position information signal (A).
$K_{\hat{p}}$	Equivalent proportional gain of a bang-bang controller in rotor position estimator.
$K_{P\hat{\omega}}, K_{I\hat{\omega}}$	Proportional and integral gains of proportional-integral (PI) controller in rotor position estimator, respectively.
K_{ω}	Band of bang-bang controller.
R	Resistance (Ω).

$R(\theta)$	Coordinate transformation matrix
$R(\theta) = \begin{bmatrix} \cos\theta & \sin\theta \\ -\sin\theta & \cos\theta \end{bmatrix}$	
L	Inductance (H).
$T(\theta)$	Coordinate transformation matrix from three-phase reference frame to synchronous reference frame.
T_e	Electromagnetic torque (N · m).
V_{inj}, ω_h	Magnitude (V) and frequency (rad/s) of injected high-frequency voltage, respectively.
V_{DC}	DC-link voltage (V).
j	Operator ($1 \angle \pi/2$).
p	Differential operator (d/dt).
λ	Flux linkage (Wb·turns).
θ_r, θ_{rm}	Actual rotor position (electrical and mechanical angle) (rad), respectively.
$\hat{\theta}_r$	Estimated rotor position (electrical) (rad).
θ_r	Rotor position estimation error (electrical) (rad).
ω_r	Actual rotor speed (rad/s).
ω_{rpm}	Actual rotor speed (r/min).
$\hat{\omega}_r$	Estimated rotor speed (rad/s).

Subscripts

PM	Permanent-magnet quantity.
avg	Average value between d and q axes.
c	Cross-coupling component.
$diff$	Difference value between d and q axes.
d, q	d and q axes, respectively.
$1, h$	Fundamental and high-frequency components, respectively.
s	Stator quantity.

Superscripts

r	Actual rotor reference frame.
\hat{r}	Estimated rotor reference frame.
$*$	Reference value.

I. INTRODUCTION

AN ESSENTIAL requirement in controlling permanent-magnet (PM) machines is to determine the rotor position information, because the rotor flux of a PM machine is from the permanent magnet attached to the rotor. Position sensors such as the resolver or the absolute encoder are required

Paper IPCSD-04-046, presented at the 2003 Industry Applications Society Annual Meeting, Salt Lake City, UT, October 12–16, and approved for publication in the IEEE TRANSACTIONS ON INDUSTRY APPLICATIONS by the Industrial Drives Committee of the IEEE Industry Applications Society. Manuscript submitted for review July 1, 2003 and released for publication June 28, 2004.

J.-H. Jang and S.-K. Sul are with the School of Electrical Engineering/Computer Engineering, College of Engineering, Seoul National University, Seoul 151-744, Korea (e-mail: bluemat@eepel.snu.ac.kr; sulsk@plaza.snu.ac.kr).

J.-I. Ha is with the Mechatronics Center, Samsung Electronics Company, Ltd., Suwon 442-742, Korea (e-mail: jungik.ha@samsung.com).

M. Ohto and K. Ide are with the Mechatronics R&D Department, Corporate R&D Center, Yaskawa Electric Corporation, Kitakyushu-City 803-8530, Japan (e-mail: ohto@yaskawa.co.jp; kozo@yaskawa.co.jp).

Digital Object Identifier 10.1109/TIA.2004.836222

in a high-performance PM machine drive system in order to determine the rotor position. However, in many industrial applications, the presence of such a position sensor reveals several disadvantages in the areas of cost, reliability, machine size, and noise interference. Therefore, there has been much research on eliminating the position sensor mounted to the rotor of the PM machines by obtaining the rotor position information indirectly.

Back-electromotive-force (EMF) estimation-based sensorless control schemes have been developed in order to determine the rotor position and speed of a PM machine without position sensors [1]–[7]. These schemes show good performance in the medium-to-high-speed range. However, the common problem of these schemes is that the performance is dependent on the rotor speed because the magnitude of back-EMF voltage is proportional to the rotor speed. This fact causes the variation of the signal-to-noise ratio (SNR) according to the rotor speed and degrades the performance of the back-EMF-based schemes when the rotor rotates at a low speed or stands still, because the magnitude of the back-EMF voltage is very small or zero. Recently, in order to overcome the drawbacks of these schemes, some estimation schemes based on the saliency phenomena of PM machines have been developed [8]–[13]. In these schemes, various types of extra signals are injected into the machines in order to detect the saliency phenomena by superimposing to the fundamental excitation signals. However, regardless of the type of injected extra signal, the analysis for the surface-mounted PM (SMPM) machine has not been fully performed.

This paper presents the analysis of an SMPM machine in regard to the sensorless operation based on the high-frequency fluctuating voltage signal injection method. This sensorless control scheme is not based on the saturation from the fundamental excitation but is based on the magnetic saliency due to the saturation from the PM flux by injecting a high-frequency voltage signal in order to detect the magnetic saliency.

This paper is organized as follows. In Section II, a simplified high-frequency model of the SMPM machine in the estimated rotor reference frame is developed, and a sensorless control scheme based on the high-frequency impedance difference is described in Section III. In Section IV, the high-frequency impedance characteristics are analyzed using finite-element analysis (FEA) and measurements under various signal injection conditions. The analysis results show that the information containing the rotor position estimation error can be obtained based on the simplified model at high frequency. Finally, the experimental results using a commercial SMPM machine are presented in Section V.

II. SIMPLIFIED HIGH-FREQUENCY MODEL OF SMPM MACHINE

Equation (1) presents the voltage equations of an SMPM machine in the actual rotor reference frame

$$\begin{bmatrix} v_{ds}^r \\ v_{qs}^r \end{bmatrix} = \begin{bmatrix} R_s + L_s p & -\omega_r L_s \\ \omega_r L_s & R_s + L_s p \end{bmatrix} \begin{bmatrix} i_{ds}^r \\ i_{qs}^r \end{bmatrix} + \begin{bmatrix} 0 \\ \omega_r \lambda_{PM} \end{bmatrix}. \quad (1)$$

If the high-frequency components in (1) are only considered by assuming that a high-frequency signal is injected into the machine, the back-EMF voltage (the second term on the right-hand side of (1)) can be neglected because it does not have

any high-frequency component. It should be noted that diagonal terms in the impedance matrix in (1) include terms proportional to the time derivative of currents, but cross-coupling terms (off-diagonal terms) do not have these terms. This means that the cross-coupling terms in the voltage equations can be neglected in steady state if the frequency of the injected signal is sufficiently high compared to the rotor speed because time-derivative terms of current are proportional to the high frequency. Based on the simplification, the high-frequency components of the voltage equations of an SMPM machine can be expressed as (2)

$$\begin{bmatrix} v_{dsh}^r \\ v_{qsh}^r \end{bmatrix} = \begin{bmatrix} r_{dh}^r + L_{dh}^r p & 0 \\ 0 & r_{qh}^r + L_{qh}^r p \end{bmatrix} \begin{bmatrix} i_{dsh}^r \\ i_{qsh}^r \end{bmatrix} \quad (2)$$

where v_{dsh}^r , v_{qsh}^r and i_{dsh}^r , i_{qsh}^r are the high-frequency components of d - and q -axes voltages and currents in the actual rotor reference frame, respectively. r_{dh}^r , r_{qh}^r and L_{dh}^r , L_{qh}^r are d - and q -axes resistances and inductances at high frequency in the actual rotor reference frame, respectively.

Equation (2) can be expressed as (3) using the frequency of the injected high-frequency voltage signal ω_h in steady state

$$\begin{aligned} \begin{bmatrix} v_{dsh}^r \\ v_{qsh}^r \end{bmatrix} &= \begin{bmatrix} r_{dh}^r + j\omega_h L_{dh}^r & 0 \\ 0 & r_{qh}^r + j\omega_h L_{qh}^r \end{bmatrix} \begin{bmatrix} i_{dsh}^r \\ i_{qsh}^r \end{bmatrix} \\ &\equiv \begin{bmatrix} z_{dh}^r & 0 \\ 0 & z_{qh}^r \end{bmatrix} \begin{bmatrix} i_{dsh}^r \\ i_{qsh}^r \end{bmatrix} \end{aligned} \quad (3)$$

where z_{dh}^r and z_{qh}^r are the d - and q -axes high-frequency impedances in the actual rotor reference frame, respectively.

In sensorless operation, the estimated rotor reference frame should be used instead of the actual one because the actual rotor position cannot be known. The high-frequency voltage equations in the estimated rotor reference frame can be expressed as (5) by transforming (3) with the definition of rotor position estimation error as in (4)

$$\begin{aligned} \tilde{\theta}_r &\equiv \theta_r - \hat{\theta}_r. \\ \begin{bmatrix} \hat{v}_{dsh}^r \\ \hat{v}_{qsh}^r \end{bmatrix} &= R(\tilde{\theta}_r)^{-1} \begin{bmatrix} z_{dh}^r & 0 \\ 0 & z_{qh}^r \end{bmatrix} R(\tilde{\theta}_r) \begin{bmatrix} \hat{i}_{dsh}^r \\ \hat{i}_{qsh}^r \end{bmatrix} \\ &= \begin{bmatrix} z_{avg} + \frac{z_{diff}}{2} \cos 2\tilde{\theta}_r & \frac{z_{diff}}{2} \sin 2\tilde{\theta}_r \\ \frac{z_{diff}}{2} \sin 2\tilde{\theta}_r & z_{avg} - \frac{z_{diff}}{2} \cos 2\tilde{\theta}_r \end{bmatrix} \begin{bmatrix} \hat{i}_{dsh}^r \\ \hat{i}_{qsh}^r \end{bmatrix} \end{aligned} \quad (4)$$

where z_{avg} and z_{diff} are the average and difference of d - and q -axes high-frequency impedances defined as (6), respectively,

$$z_{avg} \equiv \frac{z_{dh}^r + z_{qh}^r}{2}, \quad z_{diff} \equiv z_{dh}^r - z_{qh}^r. \quad (6)$$

After the high-frequency voltage equations in the estimated rotor reference frame are obtained, a high-frequency model of the SMPM machine in the estimated rotor reference frame can be constructed as (7). It should be noted that the impedance matrix in the estimated rotor reference frame has cross-coupling terms even though there are no such terms in the impedance matrix in the actual rotor reference frame [compare (7) with (3)]

$$\begin{bmatrix} \hat{v}_{dsh}^r \\ \hat{v}_{qsh}^r \end{bmatrix} = \begin{bmatrix} \hat{z}_{dh}^r & \hat{z}_{ch}^r \\ \hat{z}_{ch}^r & \hat{z}_{qh}^r \end{bmatrix} \begin{bmatrix} \hat{i}_{dsh}^r \\ \hat{i}_{qsh}^r \end{bmatrix} \quad (7)$$

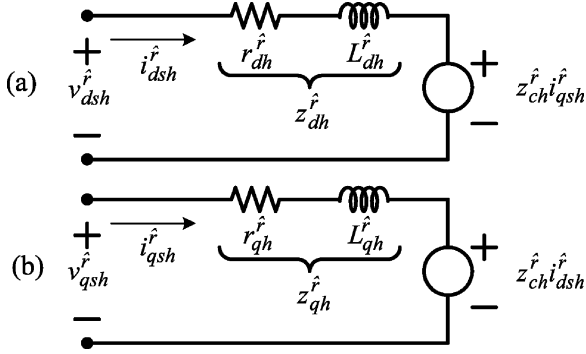


Fig. 1. SMPM model at high frequency in the estimated rotor reference frame. (a) d -axis equivalent circuit. (b) q -axis equivalent circuit.

where \hat{z}_{dh} , \hat{z}_{qh} , and \hat{z}_{ch} are d -axis, q -axis, and cross-coupling high-frequency impedances in the estimated rotor reference frame, respectively. From (5) and (7), the high-frequency impedances in the estimated rotor reference frame can be expressed as in (8)

$$\begin{aligned}\hat{z}_{dh} &\equiv z_{\text{avg}} + \frac{1}{2}z_{\text{diff}} \cos 2\tilde{\theta}_r \\ \hat{z}_{qh} &\equiv z_{\text{avg}} - \frac{1}{2}z_{\text{diff}} \cos 2\tilde{\theta}_r \\ \hat{z}_{ch} &\equiv \frac{1}{2}z_{\text{diff}} \sin 2\tilde{\theta}_r.\end{aligned}\quad (8)$$

All the high-frequency impedances in the estimated rotor reference frame are functions of the rotor position estimation error. Particularly, the cross-coupling high-frequency impedance in the estimated rotor reference frame (\hat{z}_{ch}) is proportional to the “sine” function of the rotor position estimation error ($\tilde{\theta}_r$) if the high-frequency impedance difference is not zero. This means that the actual rotor position can be estimated by forcing the cross-coupling high-frequency impedance to zero. Fig. 1 shows the d - and q -axes equivalent circuits of an SMPM machine at high frequency in the estimated rotor reference frame.

III. SENSORLESS CONTROL SCHEME

In Section II, it was shown that the cross-coupling high-frequency impedance can be used in rotor position estimation provided that the high-frequency impedance difference is not zero. However, in order to use the cross-coupling high-frequency impedance directly, it is required to know both the high-frequency voltage information and the high-frequency current information very accurately. If the high-frequency voltage information is obtained from the controller, the information is inevitably subject to the error due to the nonlinear characteristics of the pulsewidth-modulation (PWM) inverter, such as dead time and zero-current-clamping phenomena. Voltage sensors to obtain the high-frequency voltage information would increase the system cost. Even though voltage sensors are used, there are undesirable phase delays because some filters should be used in order to filter out the PWM harmonics. However, the high-frequency current information can be easily obtained using current sensors which are already part of the drive system. Therefore, an alternative method based only on the high-frequency current information is described in this section [13].

The high-frequency voltage equations in (7) can be expressed as in (9) with regard to the high-frequency currents by using the relationships between high-frequency impedances in (6) and (8)

$$\begin{aligned}\begin{bmatrix} \hat{i}_{dsh} \\ \hat{i}_{qsh} \end{bmatrix} &= \frac{1}{\hat{z}_{dh}\hat{z}_{qh} - \hat{z}_{ch}^2} \begin{bmatrix} \hat{z}_{qh} & -\hat{z}_{ch} \\ -\hat{z}_{ch} & \hat{z}_{dh} \end{bmatrix} \begin{bmatrix} \hat{v}_{dsh} \\ \hat{v}_{qsh} \end{bmatrix} \\ &= \frac{1}{\hat{z}_{dh}^r \hat{z}_{qh}^r} \begin{bmatrix} \hat{z}_{qh}^r & -\hat{z}_{ch}^r \\ -\hat{z}_{ch}^r & \hat{z}_{dh}^r \end{bmatrix} \begin{bmatrix} \hat{v}_{dsh} \\ \hat{v}_{qsh} \end{bmatrix}.\end{aligned}\quad (9)$$

In order to use the voltage and current relationships through the cross-coupling high-frequency impedance, there are two possible injection and estimation schemes using the high-frequency current information as follows.

- The fluctuating high-frequency voltage signal is injected only on the d axis in the estimated rotor reference frame as in (10) and high-frequency current on the q axis in the estimated rotor reference frame is used

$$\begin{bmatrix} \hat{v}_{ds} \\ \hat{v}_{qs} \end{bmatrix} = \begin{bmatrix} V_{\text{inj}} \cos \omega_h t \\ 0 \end{bmatrix}.\quad (10)$$

- The fluctuating high-frequency voltage signal is injected only on the q axis in the estimated rotor reference frame as in (11) and high-frequency current on the d axis in the estimated rotor reference frame is used

$$\begin{bmatrix} \hat{v}_{ds} \\ \hat{v}_{qs} \end{bmatrix} = \begin{bmatrix} 0 \\ V_{\text{inj}} \cos \omega_h t \end{bmatrix}.\quad (11)$$

In (10) and (11), V_{inj} and ω_h are magnitude and frequency of the injected high-frequency voltage signal, respectively. Between the two injection algorithms, injection of the fluctuating high-frequency voltage signal only on the d axis is better than injection of the signal only on the q axis in regard to torque ripples and additional losses from the high-frequency currents. High-frequency voltage generates high-frequency current on the same axis. Therefore, if the high-frequency voltage is injected on the estimated q axis, it generates substantial ripple torque when the rotor position estimation error is small. The tested SMPM machine has larger d -axis high-frequency impedance than q -axis high-frequency impedance as described in Section IV. This means that the magnitude of high-frequency current is larger when high-frequency voltage is injected only on the estimated q axis than when high-frequency voltage is injected only on the estimated d axis, provided that the estimated rotor position is small. Based on these facts, the high-frequency voltage signal is injected only on the d axis in the estimated rotor reference frame and the q -axis high-frequency current in the estimated rotor reference frame is used in the rotor position and speed estimation scheme described in this paper.

From (8)–(10), the q -axis high-frequency current in the estimated rotor reference frame can be expressed as in (12)

$$\begin{aligned}\hat{i}_{qsh} &= \frac{-\hat{z}_{ch}^r}{\hat{z}_{dh}^r \hat{z}_{qh}^r} V_{\text{inj}} \cos \omega_h t \\ &= -\frac{1}{2} \frac{(r_{\text{diff}} + j\omega_h L_{\text{diff}}) V_{\text{inj}} \sin 2\tilde{\theta}_r}{(r_{dh}^r + j\omega_h L_{dh}^r)(r_{qh}^r + j\omega_h L_{qh}^r)} \cos \omega_h t.\end{aligned}\quad (12)$$

In (12), r_{diff} and L_{diff} are the differences between the d - and q -axes high-frequency resistances and high-frequency inductance, respectively. If the high-frequency impedances from the high-frequency inductances are sufficiently larger than the high-frequency impedances from the high-frequency resistances, the q -axis high-frequency current in the estimated rotor reference frame can be expressed as in (13). The approximation used in (13) is verified by calculation of high-frequency resistance and inductance based on the high-frequency measurements in Section IV

$$\hat{i}_{qsh}^r \approx \frac{V_{\text{inj}}}{2} \left[\frac{r_{\text{diff}} \cos \omega_h t}{\omega_h^2 L_{dh}^r L_{qh}^r} - \frac{\omega_h L_{\text{diff}} \sin \omega_h t}{\omega_h^2 L_{dh}^r L_{qh}^r} \right] \sin 2\tilde{\theta}_r. \quad (13)$$

The sensorless control scheme uses only the second term on the right-hand side of (13) [13]. This utilization has mainly two characteristics, as follows.

- The saturation effect due to the PM flux is more effective on the inductance than resistance. Therefore, the inductance difference is more significant than the resistance difference. This makes the utilization of the second term in (13) more effective than the utilization of first term or utilization of both terms.
- The second term in (13) is orthogonal to the injected high-frequency voltage signal. Therefore, the effect of simplification described in Section II [simplification from (1) to (2)] is not significant because the high current component from the cross-coupling term has negative phase from the injected high-frequency voltage, provided that the high-frequency inductances are dominant in the high-frequency impedance. Furthermore, the magnitude of the cross-coupling term is very small compared to the diagonal term. The effect of the neglected term is increased as the rotor speed increases and can deteriorate the rotor position estimation. However, the main constraint of this sensorless control scheme is not from the rotor speed effect itself but from the insufficient voltage due to increasing back-EMF voltage.

In order to obtain the rotor position estimation error from (13), a signal processing method using a bandpass filter (BPF), a multiplication, and a low-pass filter (LPF) is used as follows.

- A BPF is used in order to extract the injected frequency component from the q -axis current in the estimated rotor reference frame.
- A multiplication is used in order to extract the orthogonal term to the injected high-frequency voltage from the high-frequency current.
- An LPF is used to eliminate the second-order harmonic term in the obtained signal.

The high-frequency component of q -axis current in the estimated rotor reference frame in (13) is obtained through a BPF. If a signal is multiplied by this high-frequency component of q -axis current as in (14), a signal consisting of two components can be obtained. The two components are a dc component and a second-order harmonic component. Therefore, a signal containing the rotor position estimation error can be obtained if the

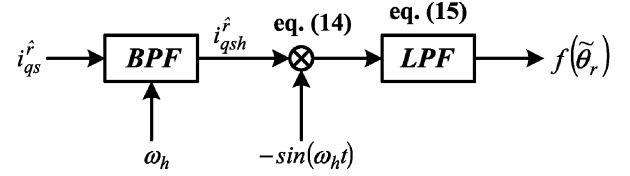


Fig. 2. Block diagram of signal processing.

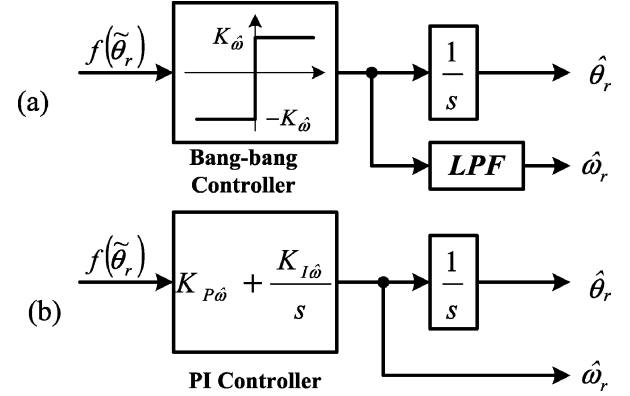


Fig. 3. Block diagram of rotor position and speed estimation. (a) Bang-bang controller and integrator. (b) PI regulator and integrator.

signal in (14) is passed through an LPF with appropriate corner frequency

$$-\hat{i}_{qsh}^r \sin \omega_h t = \frac{V_{\text{inj}} \sin 2\tilde{\theta}_r}{2\omega_h^2 L_{dh}^r L_{qh}^r} \left[\frac{\omega_h L_{\text{diff}}}{2} - |z_{\text{diff}}| \sin(2\omega_h t - \phi) \right] \quad (14)$$

where $|z_{\text{diff}}| = \sqrt{r_{\text{diff}}^2 + (\omega_h L_{\text{diff}})^2}$ and $\tan \phi = (\omega_h L_{\text{diff}}/r_{\text{diff}})$.

$$f(\tilde{\theta}_r) \equiv \text{LPF} [-\hat{i}_{qsh}^r \sin \omega_h t] = \frac{V_{\text{inj}} L_{\text{diff}}}{4\omega_h L_{dh}^r L_{qh}^r} \sin 2\tilde{\theta}_r. \quad (15)$$

If the rotor position estimation error is sufficiently small, the input signal in (15) can be approximated as in (16)

$$f(\tilde{\theta}_r) \approx \frac{V_{\text{inj}} L_{\text{diff}}}{2\omega_h L_{dh}^r L_{qh}^r} \tilde{\theta}_r \equiv K_{\text{err}} \tilde{\theta}_r. \quad (16)$$

Fig. 2 shows the block diagram of a signal processing procedure to obtain the rotor position estimation error information. It can be noted that the signal processing procedure does not use any additional information. The q -axis current in the estimated rotor reference frame is already obtained because it should be used in the synchronous reference frame current controller.

In order to estimate the rotor position and speed from rotor position estimation error information in (16), a rotor position and speed estimator should be used. Various rotor position estimators can be used as the rotor position and speed estimator; two examples are described in this paper as in Fig. 3.

Fig. 3(a) shows the block diagram of the rotor position and speed estimator when a bang-bang controller and an integrator are used to estimate the rotor position. A bang-bang controller can be regarded as a proportional controller with variable gain.

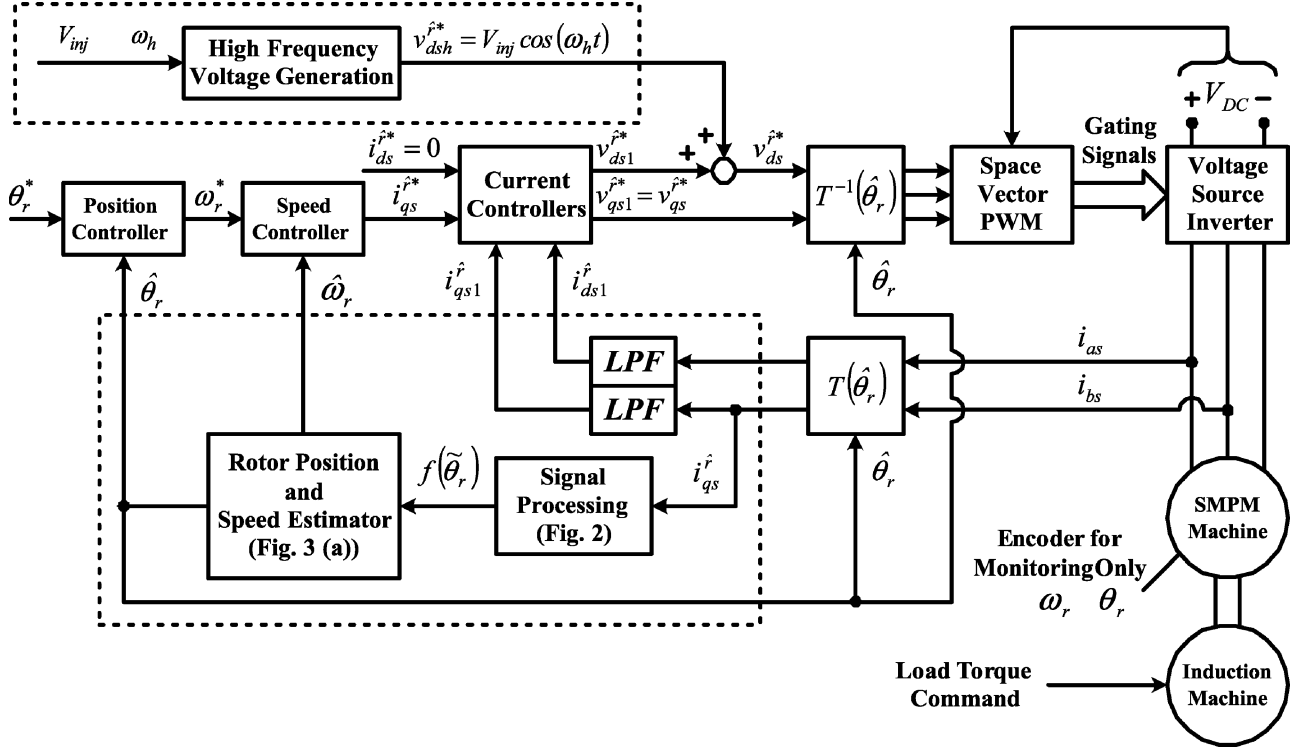


Fig. 4. Block diagram of sensorless drive system of an SMPM machine.

Therefore, the transfer function from the actual rotor position to the estimated one can be expressed as in (17)

$$\frac{\hat{\theta}_r}{\theta_r} = \frac{K_{\hat{P}} K_{err}}{s + K_{\hat{P}} K_{err}} \quad (17)$$

where $K_{\hat{P}}$ is the equivalent proportional gain of the bang-bang controller. Because the output of the bang-bang controller is fixed, the equivalent proportional gain is varied according to the magnitude of the input signal $f(\tilde{\theta}_r)$. Also, the dynamics of the output of the bang-bang controller are limited by the width of the bang-bang controller $K_{\hat{\omega}}$. If a bang-bang controller is used as the rotor position estimator, the rotor speed can be obtained from the output of the bang-bang controller. An LPF filter should be used in order to reduce the ripples contained in the output of the bang-bang controller.

Fig. 3(b) shows the block diagram of the rotor position and speed estimator when a PI controller and an integrator are used to estimate the rotor position. If a PI controller and an integrator are used as the rotor position estimator, the transfer function from the actual rotor position to the estimated one can be expressed as in (18)

$$\frac{\hat{\theta}_r}{\theta_r} = \frac{K_{P\hat{\omega}} K_{err} s + K_{I\hat{\omega}} K_{err}}{s^2 + K_{P\hat{\omega}} K_{err} s + K_{I\hat{\omega}} K_{err}} \quad (18)$$

The transfer function in (18) has a unity gain in steady state, which means that the rotor position can be estimated without error in steady state. In this case, the rotor speed can be obtained from the output of the PI controller without an LPF because the output of the PI controller does not have much ripple.

Fig. 4 shows the block diagram of the control scheme for sensorless operation of an SMPM machine. A P controller and a

PI controller for position and speed control are used, respectively. Currents are controlled by a synchronous PI controller with cross-coupling decoupling and back-EMF compensation. In the figure, cross-coupling decoupling and back-EMF compensation parts are not presented for a clear view. Feedback currents for current controllers are obtained through two LPFs after measured currents are transformed to the estimated rotor reference frame. The d -axis current reference is set to zero because it does not contribute to torque production in an SMPM machine, and the q -axis current reference is set according to the torque reference which is the output of the speed controller. Load torque is applied by a vector-controlled induction machine rigidly coupled to the tested SMPM machine. Areas enclosed by dotted rectangles in the figure are additional parts for sensorless operation. They are high-frequency voltage signal injection parts, and two LPFs, and signal processing and rotor position and speed estimation parts. All the additional parts are implemented in the software.

IV. ANALYSIS OF HIGH-FREQUENCY IMPEDANCE OF THE SMPM MACHINE

In Section II, a simplified high-frequency model of the SMPM machine in the estimated rotor reference frame was developed, and a sensorless control scheme based on the cross-coupling high-frequency impedance containing the rotor position estimation error information was described in Section III. The essential requirement for this sensorless control scheme is the high-frequency impedance difference between d and q axes in the rotor reference frame. In this section, the high-frequency impedances of an SMPM machine are analyzed by FEA and compared by measurement using the PWM inverter

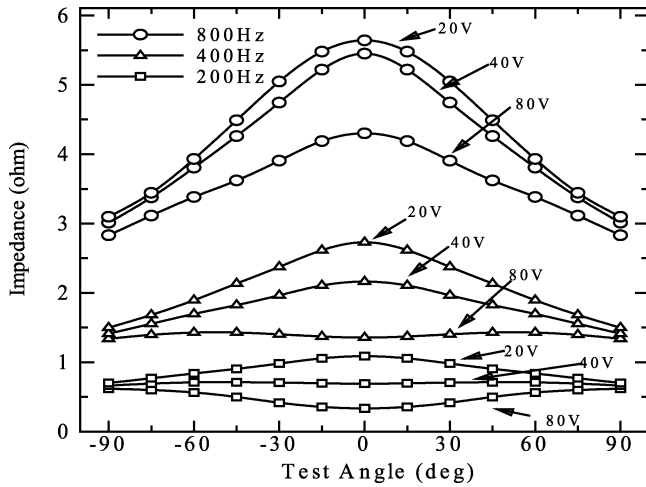


Fig. 5. High-frequency impedances under various injection conditions (finite-element analysis results).

system in order to support the sensorless control scheme. In the analyses of the high-frequency impedance characteristics of the SMPM machine, a commercial SMPM machine has been used. The parameters of the tested SMPM machine are provided in Table II. In the high-frequency impedance analyses, the high-frequency signal is injected on the “Test Angle” in Figs. 5, 7, and 8 which means the difference between the measurement axis and the actual d axis of the machine [this is the negation of the rotor position estimation error defined in (4)]. When the “Test Angle” is zero, the high-frequency signal is injected on the actual d axis, and when “Test Angle” is 90° , the high-frequency signal is injected on the actual q axis.

A. FEA

Fig. 5 shows the high-frequency impedance characteristics of the tested SMPM machine obtained by FE simulations under various injection conditions. The magnitudes of the injected high-frequency voltage signal have been set to 20, 40, and 80 V, respectively, and the frequencies have been set to 200, 400, and 800 Hz. From the figure, it can be known that the inductance component is dominant in high-frequency impedance because the high-frequency impedance is increased according to the frequency of the injected signal with the same magnitude. The figure also shows that the variation of the d -axis high-frequency impedances is much larger than the variation of the q -axis high-frequency impedances when the magnitude of the injected high-frequency signal is varied.

These can be explained using the high-frequency flux path and the physical location of windings as in Fig. 6. Fig. 6 shows the physical locations of windings and flux paths in a two-pole SMPM machine. Actual d -axis windings are located in the q axis, and q -axis windings are located in the d axis in the rotor reference frame. Because the high-frequency flux passes through the stator leakage path, resultant flux from high-frequency voltage injected on the d axis passes as *flux B* in the figure, and resultant flux from high-frequency voltage injected on the q axis passes as *flux A* in the figure. Therefore, d -axis inductance is larger than q -axis inductance because *flux A* passes through the highly saturated part of the stator. This

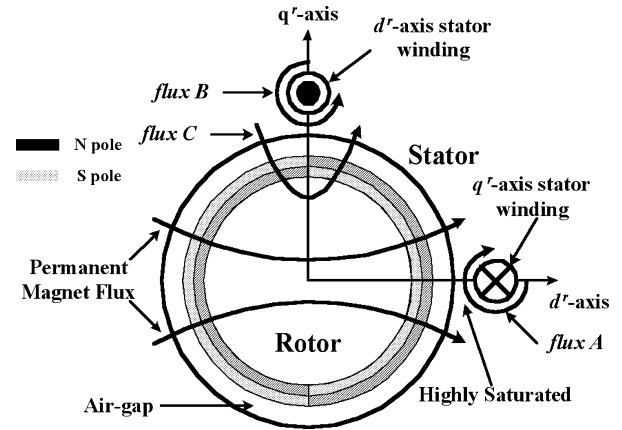


Fig. 6. Physical location of windings and flux paths in two-pole SMPM machine.

is the difference between the inductance characteristics in the fundamental component and in the high-frequency component. In Fig. 5, it can be observed that the impedance characteristics are reversed when the high-frequency voltage has high magnitude and low frequency such as 80 V–200 Hz and 80 V–400 Hz. This is because some of the flux paths are changed. When the magnitude of the high-frequency voltage signal injected on the d axis becomes large, some fluxes can pass through the air gap and rotor because the density of the main flux is not so high where the d -axis winding is located. Therefore, some of the resultant flux from d -axis injection can pass as *flux C* in the figure. However, the resultant flux from q -axis injection cannot pass as this is due to high flux density around the winding. Therefore, the d -axis inductance is smaller than the q -axis inductance. This effect can be observed in Fig. 5 if 200-Hz injection conditions are considered. When the frequency of the signal is 200 Hz, q -axis impedance is a little bit decreased when the magnitude of injected voltage increases due to the variation of the saturation level. However, d -axis impedance is substantially decreased due to the change of the flux path.

B. Measurement by PWM Inverter System

For comparison with the FEA results and investigating the high-frequency impedance characteristics in a real case, high-frequency impedance characteristics of the same SMPM machine have been measured using a PWM inverter system. In order to measure the high-frequency impedances, the rotor shaft of the SMPM machine is mechanically locked and a high-frequency voltage signal is injected using a PWM inverter, and the currents are measured using Hall-effect current sensors and processed using a digital signal processor (DSP). The detailed procedure of high-frequency impedance measurement is described in [13].

Fig. 7 shows the measured high-frequency impedance characteristics. Injection conditions of 200 Hz and 80 V–400 Hz have not been performed due to the mechanical resonance problem. Even though these injection conditions are not investigated, the provided measurement results can show a tendency similar to the FEA results. The high-frequency impedances in Fig. 7 are somewhat different from the high-frequency impedances in Fig. 6 in absolute value. This is from the nonideal

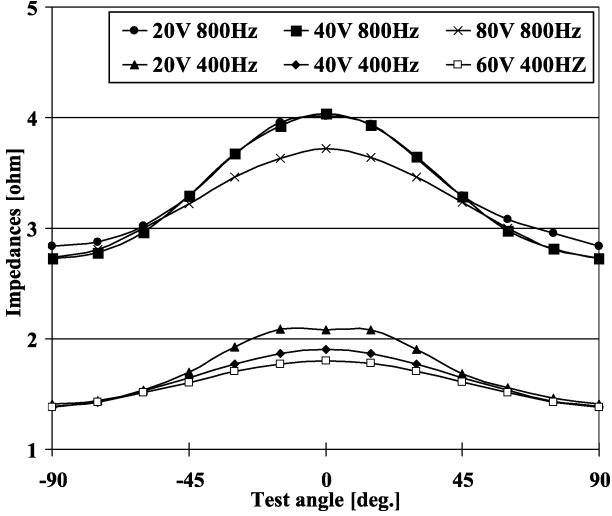


Fig. 7. High-frequency impedances under various injection conditions (measurement results).

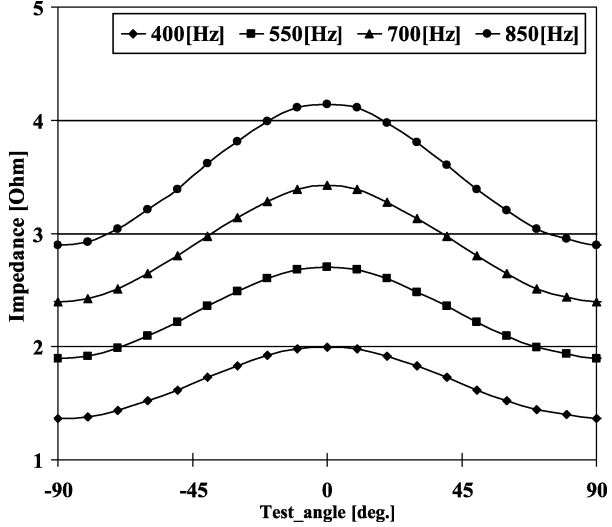


Fig. 8. High-frequency impedances under various injection frequencies (measurement results, 40 V).

effect of the PWM inverter system and inevitable errors in digital signal processing. However, the impedance characteristics are the same as the FEA results. As the frequency of injected high-frequency voltage increases, the impedances are also increased. This supports the view that the inductance component is dominant in the high-frequency impedance. At the same frequency, the d -axis high-frequency impedances are larger than the q -axis high-frequency impedances. Fig. 8 shows the high-frequency impedance characteristics obtained by measurements under various injection frequencies with fixed magnitude (40 V). From Fig. 8, it can be calculated the d - and q -axes high-frequency inductances and resistances using the definition in (3). The calculated high-frequency inductances and resistances are presented in Table I. The calculated results may have some errors due to the measurement and signal processing errors. Even though some errors are considered, it can be noted that the high-frequency inductances are dominant and the high-frequency resistance difference is very small.

TABLE I
HIGH-FREQUENCY RESISTANCES AND INDUCTANCES

	Resistance [Ω]	Inductance [mH]	Impedance from Inductance [Ω] (850Hz)
D-axis	0.347	0.780	4.17
Q-axis	0.354	0.541	2.88
Difference	-0.007	0.239	1.29

C. Analysis of FEA and Measurement Results

The high-frequency impedance characteristics by the FEA results and by the measurement results agree with each other with the exception of the absolute value of the high-frequency impedance. The following facts can be deduced from the results.

- The high-frequency inductance component is dominant in the high-frequency impedance. This supports the assumption used in developing (13).
- The d -axis high-frequency impedance is larger than the q -axis high-frequency impedance under appropriate injection conditions. Also, this supports the selection of the d -axis injection in the sensorless control algorithm.
- The high-frequency impedance difference is higher when the injected high-frequency voltage signal has smaller magnitude and higher frequency. However, an absolute value of the high-frequency impedance difference does not have any meaning itself. Because the magnitude of the signal containing the rotor position estimation error is determined by K_{err} coefficient [see (16)]. The high-frequency component of current is extracted from the measured current. If this component is small, the quantization error of an analog-to-digital (A/D) converter can distort the extracted signal. Therefore, the injection condition should be selected to make the coefficient as high as possible in order to increase the SNR. From the measurement results, this coefficient can be calculated. For example, the calculated values of it are 1.03 and 3.89 when a 20-V-800-Hz and an 80-V-800-Hz signal is injected, respectively. Therefore, an 80-V-800-Hz high-frequency signal is better than the 20-V-800-Hz signal even though the high-frequency impedance difference is smaller.
- Based on the analysis results, the basic guidelines in selecting the injection conditions in actual sensorless operation can be obtained by calculating K_{err} . However, in the experiments, other factors should be considered, such as the nonlinearity of PWM inverters, accuracy and resolution of current measurements, accuracy of the digital filters used in the signal processing, and so on [14]–[16].

V. EXPERIMENTAL RESULTS

Based on the analyses of the high-frequency impedance characteristics of the SMPM machine, experiments on sensorless operation of the SMPM machine have been performed with the control scheme of Fig. 4. In the experiments, the same SMPM machine as in the high-frequency impedance analyses (Table II) has been used. A TMS320VC33 DSP-based control board has

TABLE II
PARAMETERS OF SMPM MACHINE UNDER TEST

Rated Power	11 kW
Number of Poles	8
Rated Current	58.6 Arms
Rated Speed	1,500 r/min
Torque Coefficient	1.25 N · m/Arms
Rated Torque	70 N · m
Inertia	0.0281 kg · m ²
Resistance (per phase)	0.0217 Ω
Inductance (per phase)	0.49 mH

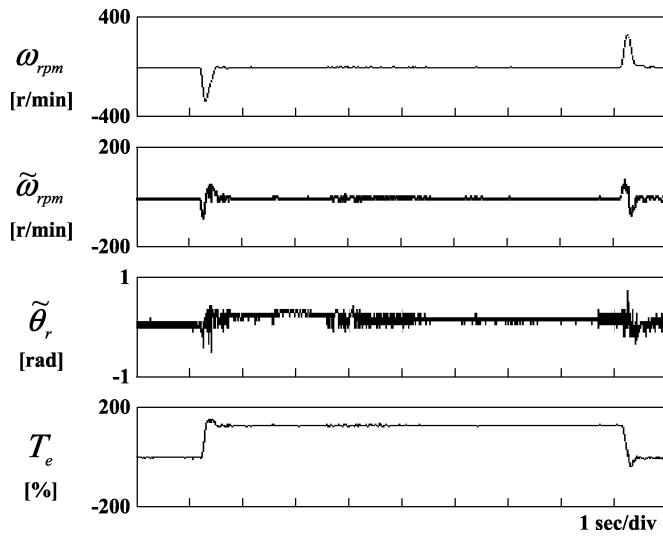


Fig. 9. Performance of sensorless speed control when the speed command is zero under 130% step load torque (from top to bottom: measured speed, rotor speed estimation error, rotor position estimation error, and torque).

been used to control the SMPM machine. The sampling frequency has been set at 10 kHz for current control and rotor position and speed estimation, and 1 kHz for speed and position control. In order to drive the SMPM machine, a three-phase inverter has been used with 5-kHz switching frequency. An 8192-pulse-per-revolution (PPR) encoder has been used to monitor the actual rotor position and speed. The injection condition has been selected as 100 V–850 Hz through a tuning process in order to achieve the speed and position control performance under step-load torque condition. Even though the selection condition is not as accurate as the analysis, the analysis results are very helpful in selecting the injection condition.

A. Sensorless Speed Control

The performance of the sensorless speed control at zero and low speed is presented in Figs. 9 and 10. The amount of the step-load torque is 130% of the rated torque of the SMPM machine. The speed commands in Figs. 9 and 10 have been set to zero and 30 r/min (2 Hz), respectively. The rotor position estimation errors in both cases are somewhat increased in transient state. However, the system does not lose controllability. The maxim rotor position estimation error in Fig. 10 is somewhat larger than in Fig. 9. This is not from the effect of the rotor speed

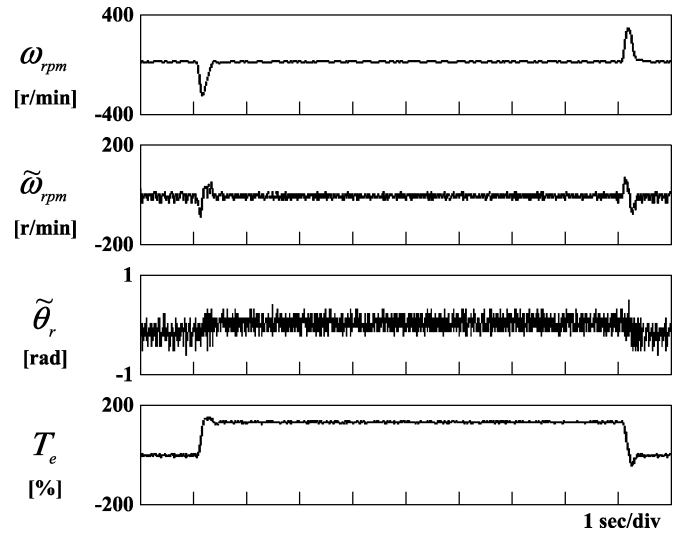


Fig. 10. Performance of sensorless speed control when the speed command is 30 r/min under 130% step load torque (from top to bottom: measured speed, rotor speed estimation error, rotor position estimation error, and torque).

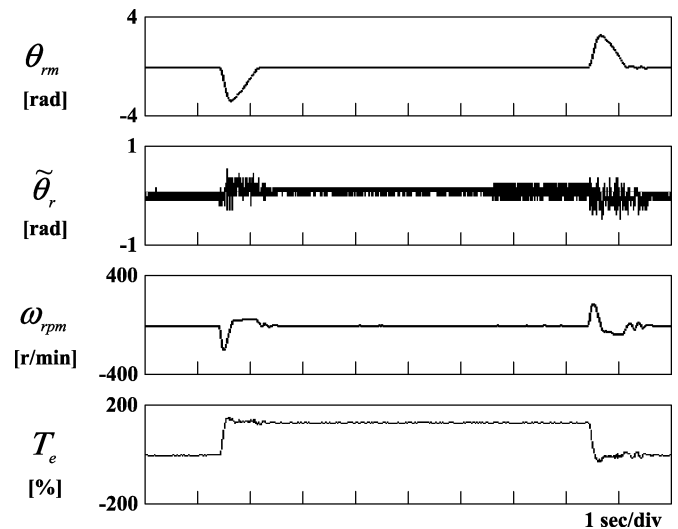


Fig. 11. Performance of sensorless position control when the position command is zero under 130% step load torque (from top to bottom: measured rotor position (mechanical), rotor position estimation error, measured rotor speed, and torque).

and position estimation but from the dead-time and zero-current-clamping effects which deteriorate the output voltage of the PWM inverter in the low-frequency region, which are very difficult to accurately compensate when high-frequency components exist.

At loaded condition, the rotor position estimation error is increased. This is because the saturated position is a little changed due to the flux from the stator current. Therefore, the performance of position estimation may be increased if the effect of stator current is considered and compensated.

B. Sensorless Position Control

The performance of the sensorless position control is presented in Figs. 11 and 12. The amount of the load torque is 130% of the rated torque as in the sensorless speed control operation.

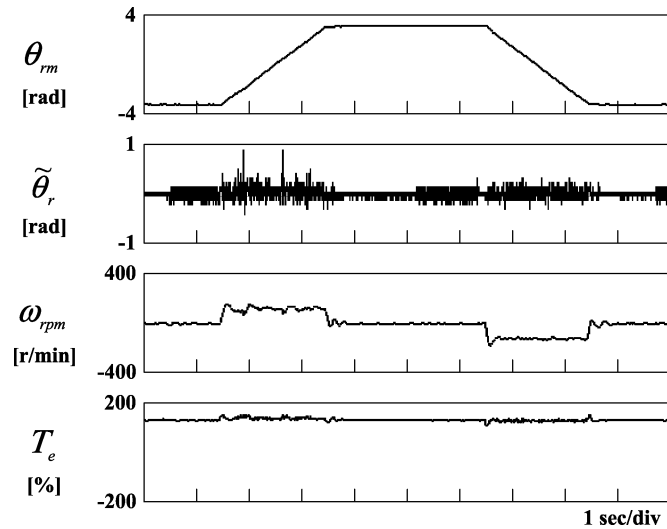


Fig. 12. Performance of sensorless position control when the mechanical position command is varying from $-\pi \sim \pi$ rad under 130% load torque (from top to bottom: measured rotor position (mechanical), rotor position estimation error, measured rotor speed, and torque).

In the operation of Fig. 11, the mechanical rotor position command has been set to zero and the step-load torque has been applied. The duration of the transient state is somewhat long because the position controller is a simple P controller whose bandwidth is low (a few hertz). The rotor position estimation error is increased at the transient state and loaded condition. However, the system does not lose controllability, even in transient state, and the estimation error is decreased in steady state.

In the operation of Fig. 12, the mechanical rotor position command has been changed from $-\pi$ rad to π rad and vice versa when constant load torque is applied. The maximum rotor speed is limited at 80 r/min. The rotor position estimation is increased when the rotor is rotating due to the dead-time and zero-current-clamping effects, which is the same tendency as in speed control operation.

VI. CONCLUSION

In this paper, the analysis of an SMPM machine for a sensorless control scheme based on the high-frequency fluctuating voltage signal injection method was presented. For the analysis, a simplified SMPM machine model at high frequency in the estimated synchronous reference frame was developed. In the model, the high-frequency impedances are represented as functions of the rotor position estimation error. Particularly, it is shown that the cross-coupling high-frequency impedance in the estimated rotor reference frame can be used in order to estimate the rotor position because it is proportional to the "sine" function of the rotor position estimation error. A sensorless control scheme based on this model was described. The sensorless control scheme does not directly use the cross-coupling impedance in the estimated rotor reference frame, but uses the high-frequency component of current.

In order to support the developed model and sensorless control scheme and to investigate the high-frequency impedance characteristics of an SMPM machine, FEA analysis and high-frequency impedance measurement using the PWM in-

verter system have been performed under various injection conditions. The high-frequency impedance analysis results show that the high-frequency inductance component is dominant, and that the d -axis high-frequency impedance is larger than the q -axis high-frequency impedance under appropriate injection conditions, and that the impedance difference is larger when the injected signal has lower magnitude and higher frequency. Based on the analysis results, the injection condition for sensorless control of an SMPM machine can be selected even though consideration of the nonlinear behaviors of the PWM inverter and measurement systems should be provided.

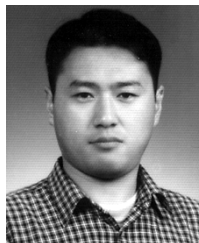
The analysis and measurement results presented in this paper show that measurement of high-frequency impedance characteristics can be used to determine the feasibility of a PM machine for sensorless operation based on the high-frequency signal injection method. This is not determined by the impedance (inductance) itself, but by the impedance difference when a high-frequency signal is injected. The performance of the sensorless control scheme for a specific PM machine is mainly dependent on the high-frequency impedance characteristics, but some system parameters such as dc-link voltage, accuracy of current measurement, and accuracy of digital filtering can affect the performance.

Experiments on the sensorless speed and position control operations based on the described rotor position and speed estimation scheme have been performed. The experimental results on the speed control and position control show satisfactory performance at low speed and zero speed even under heavy load conditions. The performances are comparable to those of sensed control when low-resolution position sensors are used, except for the ripples.

REFERENCES

- [1] L. A. Jones and J. H. Lang, "A state observer for the permanent-magnet synchronous motor," *IEEE Trans. Ind. Electron.*, vol. 36, pp. 374–382, June 1989.
- [2] R. Dhauoadi, N. Mohan, and L. Norum, "Design and implementation of an extended Kalman filter for state estimation of a permanent magnet synchronous motor," *IEEE Trans. Power Electron.*, vol. 6, pp. 491–497, June 1991.
- [3] R. Wu and G. R. Slemon, "A permanent magnet motor drive without a shaft sensor," *IEEE Trans. Ind. Applicat.*, vol. 27, pp. 1005–1011, Sept./Oct. 1991.
- [4] N. Matsui and M. Shigyo, "Brushless dc motor control without position and speed sensor," *IEEE Trans. Ind. Applicat.*, vol. 28, pp. 120–127, Jan./Feb. 1992.
- [5] J. S. Kim and S. K. Sul, "New approach for high performance PMSM drives without rotational position sensors," *IEEE Trans. Power Electron.*, vol. 12, pp. 904–911, Sept. 1997.
- [6] K. R. Shouse and D. G. Taylor, "Sensorless velocity control of permanent-magnet synchronous motors," *IEEE Trans. Contr. Syst. Technol.*, vol. 6, pp. 313–324, May 1998.
- [7] S. Bolognani, R. Oboe, and M. Zigliotto, "Sensorless full-digital PMSM drive with EKF estimation of speed and rotor position," *IEEE Trans. Ind. Electron.*, vol. 46, pp. 240–247, Apr. 1999.
- [8] P. L. Jansen and R. D. Lorenz, "Transducerless position and velocity estimation in induction and salient AC machines," *IEEE Trans. Ind. Applicat.*, vol. 31, pp. 240–247, Mar./Apr. 1995.
- [9] M. Shroedl, "Sensorless control of AC machines at low speed and standstill based on the 'INFORM' method," in *Conf. Rec. IEEE-IAS Annu. Meeting*, vol. 1, 1996, pp. 270–277.
- [10] M. J. Corley and R. D. Lorenz, "Rotor position and velocity estimation for a salient-pole permanent magnet synchronous machine at standstill and high speeds," *IEEE Trans. Ind. Applicat.*, vol. 34, pp. 784–789, July/Aug. 1998.

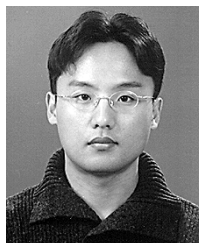
- [11] T. Aihara, A. Toba, T. Yanase, A. Mashimo, and K. Endo, "Sensorless torque control of salient-pole synchronous motor at zero-speed operation," *IEEE Trans. Power Electron.*, vol. 14, pp. 202–208, Jan. 1999.
- [12] J. I. Ha, K. Ide, T. Sawa, and S. K. Sul, "Sensorless rotor position estimation of an interior permanent-magnet motor from initial states," *IEEE Trans. Ind. Appl.*, vol. 39, pp. 761–767, May/June 2003.
- [13] J. H. Jang, S. K. Sul, J. I. Ha, K. Ide, and M. Sawamura, "Sensorless drive of surface-mounted permanent-magnet motor by high-frequency signal injection based on magnetic saliency," *IEEE Trans. Ind. Appl.*, vol. 39, pp. 1031–1039, July/Aug. 2003.
- [14] F. Briz, M. W. Degner, J. M. Guerrero, A. Zamarron, and R. D. Lorenz, "Implementation issues affecting the performance of carrier signal injection based sensorless controlled AC drives," in *Conf. Rec. IEEE-IAS Annu. Meeting*, vol. 4, 2001, pp. 2645–2652.
- [15] J. I. Ha, M. Ohto, J. H. Jang, and S. K. Sul, "Design and selection of AC machines for saliency-based sensorless control," in *Conf. Rec. IEEE-IAS Annu. Meeting*, vol. 2, 2002, pp. 1155–1162.
- [16] J. H. Jang, Y. C. Son, and S. K. Sul, "Current measurement issues in sensorless control algorithm using high frequency signal injection method," in *Conf. Rec. IEEE-IAS Annu. Meeting*, vol. 2, 2003, pp. 1134–1141.



Ji-Hoon Jang (S'01) was born in Seoul, Korea, in 1975. He received the B.S. and M.S. degrees in electrical engineering in 1999 and 2001, respectively, from Seoul National University, Seoul, Korea, where he is currently working toward the Ph.D. degree in the Power Electronics Laboratory.

Since September 2003, he has been a Visiting Scholar at the Center for Power Electronics Systems (CPES), Bradley Department of Electrical and Computer Engineering, Virginia Polytechnic Institute and State University, Blacksburg, where he

is working on the control of PM machines for starter/generator and electric pump/fan applications in aircraft systems. His current research interests are high-performance ac machine drives, sensorless drives of ac machines, and electrical systems for automotive applications.



Jung-Ik Ha (S'97–M'01) was born in Pusan, Korea, in 1971. He received the B.S., M.S., and Ph.D. degrees in electrical engineering from Seoul National University, Seoul, Korea, in 1995, 1997, and 2001, respectively.

He was with the Mechatronics R&D Department of Yaskawa Electric Company, Japan, as a Researcher from 2001 to 2002. He is currently a Senior Research Engineer with the Mechatronics Center, Samsung Electronics Company, Ltd., Suwon, Korea. His current research interests are electric machines,

drives, and electric propulsion systems.



Motomichi Ohto was born in Oita Prefecture, Japan, in 1961. He received the M.S. degree in electrical engineering from Oita University, Oita City, Japan, in 1985.

In 1986, he joined Yaskawa Electric Corporation, Kitakyushu, Japan, where he is Manager of the Mechatronics Group in the R&D Center. He is currently engaged in analysis of magnetic fields and development of new servo motor products.

Mr. Ohto is a Member of the Institute of Electrical Engineers of Japan.



Kozo Ide (S'94–M'96) received the B.S., M.S., and Ph.D. degrees in electrical engineering from Kyushu Institute of Technology, Kitakyushu, Japan, in 1991, 1993, and 1996, respectively.

From 1991 to 1992, he was a Visiting Researcher at L'Aquila University, Italy, supported by the Italian government. In 1996, he joined Yaskawa Electric Corporation, Kitakyushu, Japan, where he is currently an Assistant Manager in the R&D Center. His current research interests are control technology for ac machines and energy conversion systems.

Dr. Ide is a Member of the Institute of Electrical Engineers of Japan.



Seung-Ki Sul (S'78–M'80–SM'98–F'00) was born in Korea in 1958. He received the B.S., M.S., and Ph.D. degrees in electrical engineering from Seoul National University, Seoul, Korea, in 1980, 1983, and 1986, respectively.

From 1986 to 1988, he was an Associate Researcher with the Department of Electrical and Computer Engineering, University of Wisconsin, Madison. From 1988 to 1990, he was a Principal Research Engineer with Gold-Star Industrial Systems Company. Since 1991, he has been a member of the

faculty of the School of Electrical Engineering, Seoul National University, where he is currently a Professor. His current research interests are power-electronic control of electric machines, electric vehicle drives, custom power, and power-converter circuits.